

pubs.acs.org/JACS Article

# Regulated Electronic and Ionic Conductive Framework for High Energy Density Lithium—Sulfur Batteries

Xueting Feng,<sup>#</sup> Xuanguang Ren,<sup>#</sup> Huahui Tian,<sup>#</sup> Mingwei Cui, Guoxin Lu, Jin Zhang, and Xin Gao\*



Cite This: J. Am. Chem. Soc. 2025, 147, 30042-30049



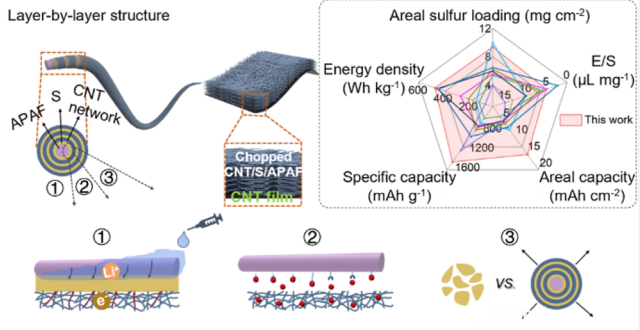
**ACCESS** 

Metrics & More

Article Recommendations

Supporting Information

ABSTRACT: Achieving high energy density in lithium—sulfur (Li–S) batteries necessitates thick cathodes with high sulfur loadings and a lean electrolyte. However, these configurations introduce critical challenges, including low conductivity, polysulfide shuttling, volume expansion, and mechanical instability, which significantly impede battery performance. In this study, we present a regulated electronic and ionic conductive framework that integrates carbon nanotubes (CNTs) and sulfur onto the surface of air plasma-treated aramid fibers (APAF) in a layer-by-layer fashion (denoted as CNT/S/APAF). This composite framework is then incorporated into a CNT network to form free-standing sulfur cathodes for high energy density Li–S batteries. The resulting structure promotes efficient electron transport, improves electro-



Facilitate electron and ion transport Confine polysulfide shuttle

Accommodate large strain

lyte wettability, suppresses polysulfide diffusion, and mitigates volume expansion. These synergistic effects lead to superior sulfur utilization and cycling stability. The Li–S cells with CNT/S/APAF cathodes exhibit an impressive initial specific capacity of 1437.6 mAh g<sup>-1</sup> and areal capacity of 11.3 mAh cm<sup>-2</sup>, with a sulfur loading of 7.83 mg cm<sup>-2</sup> and an electrolyte-to-sulfur (E/S) ratio of 5  $\mu$ L mg<sup>-1</sup>. Furthermore, they achieve a high energy density of 468.6 Wh kg<sup>-1</sup> and maintain excellent cycling stability, retaining a capacity of 6.5 mAh cm<sup>-2</sup> after 100 cycles. This scalable approach provides a practical, high-performance solution for next-generation batteries.

## INTRODUCTION

Lithium—sulfur (Li–S) batteries with their high energy density of 2600 Wh kg $^{-1}$  and low cost are regarded as a promising next-generation energy storage system.  $^{1-3}$  However, challenges such as the insulating nature of sulfur, the shuttle effect of soluble lithium polysulfides (LiPSs), and significant volume expansion limit their commercial viability.  $^{4,5}$  Recent strategies have focused on encapsulating sulfur in suitable host materials with optimized structures to address these issues by physically and/or chemically immobilizing sulfur and LiPSs.  $^{6-9}$  However, most of the performance improvements have been demonstrated at the laboratory scale, often with an insufficient sulfur content, low sulfur loading, and excess electrolyte, making it challenging to meet the high energy demands required for practical applications (energy density >400 Wh kg $^{-1}$  or cycling number >100).  $^{10,11}$ 

To achieve high energy density in Li–S batteries, thick cathodes with high sulfur loadings (>4 mg cm<sup>-2</sup>) and lean electrolyte conditions (electrolyte-to-sulfur (E/S) ratio  $\leq$  5  $\mu$ L mg<sup>-1</sup>) are essential. <sup>12–14</sup> However, several critical challenges become more pronounced under these conditions, including insulating active materials, polysulfide shuttle, and volume expansion (Figure S1). Additional kinetic barriers to the sulfur redox reactions emerge due to the low ionic conductivity caused by concentrated LiPSs. <sup>15</sup> Moreover, conventional thick

cathodes are prone to cracking and delamination during the drying process due to the high shrinkage stress of the slurry, leading to mechanical instability (Figure S1).

A flexible, free-standing cathode with highly porous and conductive carbon networks has been shown to facilitate electron and ion transport, while the introduction of polar carbon hosts (e.g., heteroatom-doped carbon or hybrids with transition metal compounds) can chemically anchor LiPSs to suppress the shuttle effect. However, these strategies often require complex functionalization and structural design of the cathode materials, limiting their practical application. Furthermore, electrolyte wettability is often overlooked in these designs, leading to insufficient ion conduction pathways and low sulfur utilization. Therefore, there is an urgent need to develop high-sulfur-loaded, flexible, free-standing cathodes with scalable production, high conductivity, and enhanced electrolyte wettability to achieve energy-dense Li–S batteries.

Received: May 4, 2025 Revised: August 2, 2025 Accepted: August 4, 2025 Published: August 11, 2025





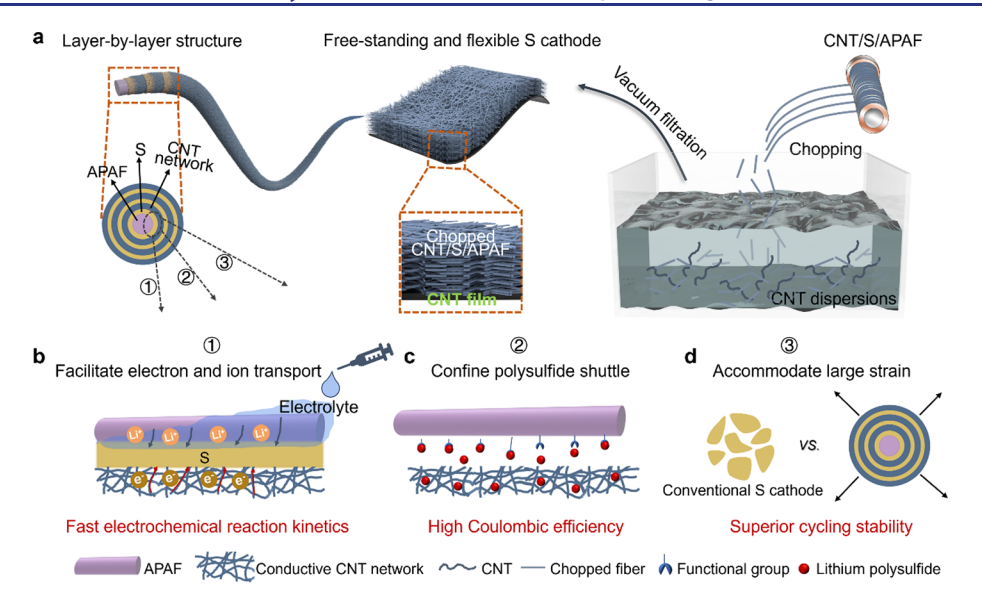


Figure 1. Preparation and design principle on CNT/S/APAF cathodes. (a) Schematic illustration showing the setup for producing CNT/S/APAF cathodes. (b) Schematic illustration of the facilitated electron and ion transport in the CNT/S/APAF cathodes. Air plasma-treated aramid fibers enhance electrolyte permeability and lithium-ion diffusion, while the conductive CNT network enhances electron transport, ensuring efficient electrochemical reactions. (c) Schematic illustration of the polysulfide shuttle confinement. Air plasma-treated aramid fibers with reactive functional groups and constructed CNT networks effectively immobilize polysulfides, reducing shuttle effects and enhancing Coulombic efficiency. (d) Schematic of morphological evolution during electrochemical cycling. Conventional S cathodes tend to pulverize during cycling, hindering sulfur redox reactions and stability. In contrast, the mechanical resilience of the aramid fibers and the flexibility of the CNTs accommodate structural stress.

In this work, we present a free-standing, flexible sulfur cathode with a regulated electronic and ionic conductive framework designed for high energy density Li—S batteries. The framework is fabricated through a layer-by-layer coating of carbon nanotubes (CNTs) and sulfur onto air plasma-treated aramid fibers (APAF), followed by fiber chopping and vacuum infiltration to form robust cathode networks (Figure S2 and Figure 1). Specifically, CNTs and sulfur are integrated onto the surface of APAF in a layer-by-layer manner, resulting in a unique composite fiber termed CNT/S/APAF. The composite fibers are chopped and mixed with a CNT dispersion to create a continuous conducting CNT network, resulting in free-standing sulfur cathodes.

Unlike traditional three-dimensional frameworks, such as carbon nanofibers, 19 which often face challenges like poor interfacial contact, limited ion diffusion, or complex synthesis procedures, the CNT/APAF composite system offers a unique combination of fast electron conduction through CNTs and efficient ion transport via the APAF structure. 20,21 The CNT network provides physical confinement for polysulfides, while the plasma treatment and chemical interactions within the aramid fibers offer additional chemical anchoring, enhancing overall polysulfide retention. Additionally, the mechanical resilience of the aramid fibers and the flexibility of the CNTs help buffer structural stress, mitigating volume expansion during cycling. This cathode design not only regulates electronic and ionic conductivity but also ensures intimate contact among the insulating sulfur, electrons, and lithium ions, thereby improving Li-S conversion kinetics and enhancing sulfur utilization. As a result, the Li-S cells with the CNT/S/APAF cathodes achieve an impressive specific capacity of 1437.6 mAh g<sup>-1</sup> and an areal capacity of 11.3 mAh cm<sup>-2</sup>, with a sulfur loading of 7.83 mg cm<sup>-2</sup> and a low E/S ratio of 5  $\mu$ L mg<sup>-1</sup>. In contrast, thick cathodes fabricated by using traditional slurry methods exhibit significantly lower performance (specific capacity: 277.4 mAh g<sup>-1</sup>; areal capacity: 1.22 mAh cm<sup>-2</sup>). Furthermore, these cells demonstrate a high cell-level specific energy of 468.6 Wh kg<sup>-1</sup>, achieved by integrating the CNT/S/APAF cathode with an ether-based electrolyte and a lithium metal anode, surpassing previously reported high-loading sulfur cathodes. The cells with CNT/S/APAF cathodes also exhibit superior cycling stability, with an average Coulombic efficiency (CE) of 98.99% over 100 cycles, along with excellent rate capability, owing to the synergistic effects of the CNT network, the active functional groups in APAF, and the unique encapsulation structure.

#### RESULTS AND DISCUSSION

Characterization of CNT/S/APAF Cathodes. First, the CNT/S/APAF was fabricated through a layer-by-layer coating process and can be directly obtained at high production rates exceeding 120 m  $h^{-1}$  (Figure 2a). The aramid fibers (AF) were treated with air plasma to activate their surface, after which sulfur and CNT were integrated onto the surface of APAF in a layerby-layer manner. X-ray photoelectron spectroscopy (XPS) surface element analysis of AF and APAF (Table S1) shows that after air plasma treatment, the carbon (C) concentration decreases, while the oxygen (O) and nitrogen (N) concentrations increase, leading to higher O/C and N/C ratios. This indicates the formation of new polar groups containing O and N. Compared to untreated fibers, higher concentrations of O= C=O and C-O groups and low concentrations of C-C are observed after treatment (Figure S3), revealing changes in the chemical composition of the AF surface.<sup>22</sup> Furthermore, the increased intensity of the C=O stretching vibration (1641 cm<sup>-1</sup>) and the decreased intensity of N-H bending (1543 cm<sup>-1</sup>) and C-N stretching (1319 cm<sup>-1</sup>) in the reflectance Fourier transform infrared (ATR-FTIR) spectra further confirm the increase in C=O (and O=C=O) groups following treatment (Figure S4). 22 These results indicate the formation of reactive functional groups on the AF after air plasma treatment, which facilitate electrolyte penetration, fast lithium-ion transfer, and the chemical anchoring of soluble LiPSs. In contrast to the

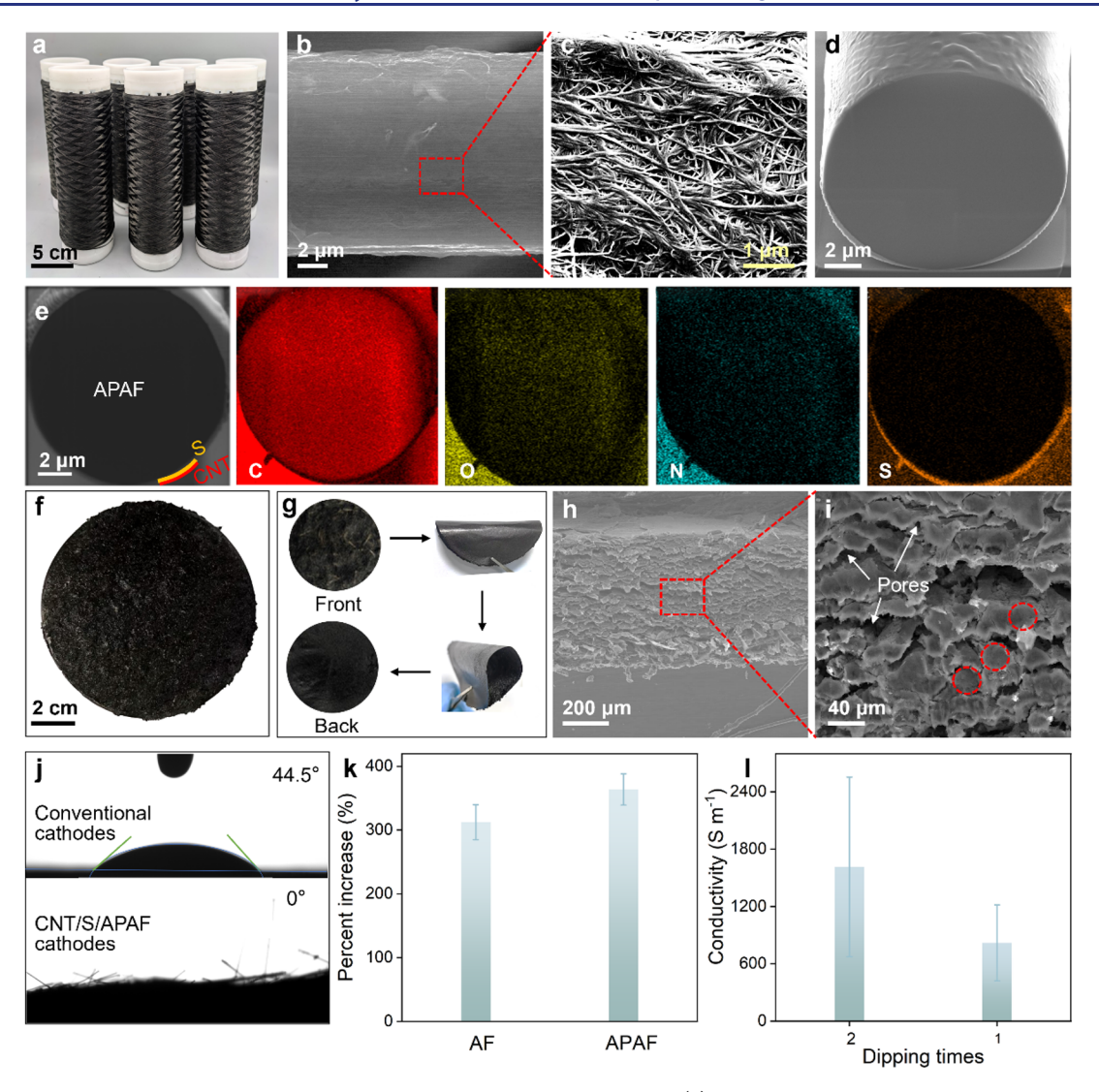


Figure 2. Morphology and properties of the CNT/S/APAF and CNT/S/APAF cathodes.(a) Digital image of continuous CNT/S/APAF. (b, c) SEM images of CNT/S/APAF. (d) Cross-sectional SEM image of CNT/S/APAF. (e) Cross-sectional scanning transmission electron microscopy (STEM) image and corresponding EDX elemental mapping of the CNT/S/APAF cathodes after one cycle of sulfur and a CNT coating. (f) Large-area CNT/S/APAF cathodes. (g) Digital images of the CNT/S/APAF cathode bending test. (h, i) Cross-sectional SEM images of CNT/S/APAF cathodes. Some fibers are indicated by the red dotted circles. (j) Contact angle of the electrolyte on the CNT/S/APAF cathodes and conventional cathodes. (k) Electrolyte wettability of AF and APAF. (l) Electrical conductivity of the CNT with different dipping times.

smooth surface of AF, the APAF exhibits an uneven surface with noticeable ruts and bulges (Figure S5), which enhances interfacial adhesion between the fiber and sulfur through physical interactions. After five sulfur and CNT alternating coating treatments, the surface of CNT/S/APAF becomes rough and is coated with a cross-linked CNT network (Figure 2b,c). The continuous CNT network not only provides electrical interconnectivity throughout the entire network but also helps anchor the LiPSs. The total diameter of the fiber is 13.8  $\mu$ m (Figure 2b and Figure S5). To further verify the successful construction of the CNT/S/APAF architecture and elucidate the spatial distribution of sulfur, cross-sectional energy-dispersive X-ray spectroscopy (EDX) line-scan analysis was conducted on the CNT/S/APAF cathodes. As shown in Figure S6, a strong sulfur signal is observed near the surface of the APAF and is continuously detected across the interfaces between APAF and CNT layers as well as between adjacent CNT layers. These results confirm the effective formation of a well-defined layer-by-layer encapsulation architecture, which is

critical for achieving high sulfur utilization and suppressing the polysulfide shuttle effect in Li-S batteries. The axial cross-sectional scanning electron microscopy (SEM) image of the fiber coated with sulfur and CNT shows a uniform and tight coating of sulfur and CNT on the fiber surface, with a thickness of 217 nm (Figure 2d). EDX mapping reveals that the O and N elements are uniformly distributed throughout the fiber, while the sulfur element is localized on the fiber surface, and carbon is distributed across the fiber (Figure 2e). These results confirm the uniform coating of sulfur and CNT on the fiber surface. Additionally, the sulfur content can be precisely controlled by adjusting the sulfur concentration, with the concentration and content being linearly correlated (Figure S7).

The prepared CNT/S/APAF is chopped, mixed with CNT dispersion, and filtered to construct a continuous conductive CNT network, yielding CNT/S/APAF cathodes. By adjusting the capacity of the filtration flask and the amount of fiber used, cathodes with varying diameters and sulfur loadings can be tailored for different applications (Figure 2f). As shown in

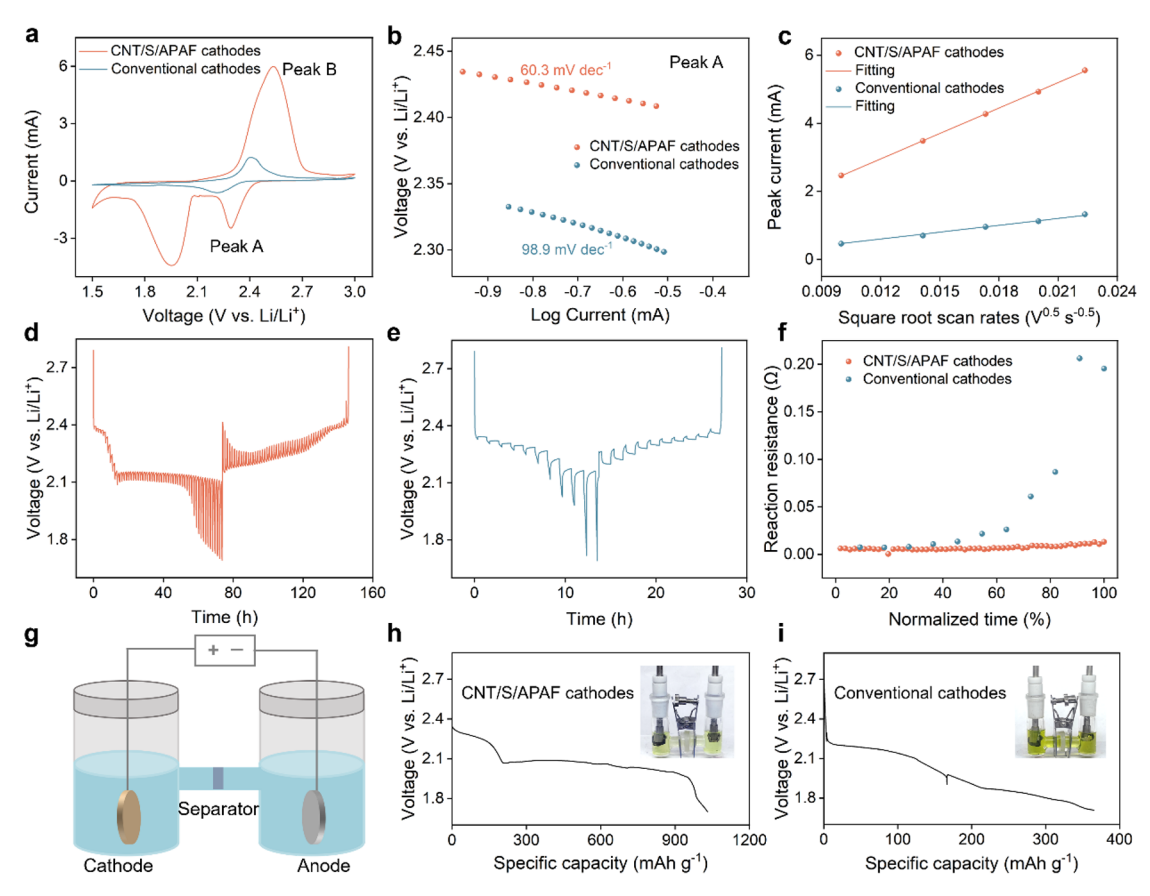


Figure 3. Electrochemical kinetics characterizations. (a) CV curves of CNT/S/APAF and conventional cathodes at 0.1 mV s<sup>-1</sup>. (b) Tafel plots were calculated from reduction peak A in panel (a). (c) Koutecky–Levich (K-L) plots of CNT/S/APAF cathodes and conventional cathodes. The GITT plots of (d) CNT/S/APAF cathodes (S: 9.40 mg cm<sup>-2</sup>) and (e) conventional cathodes (S: 4.00 mg cm<sup>-2</sup>) at a current density of 0.05 C. (f) Calculated reaction resistances of CNT/S/APAF cathodes and conventional cathodes concerning normalized discharge–charge time. (g) Schematic illustration of the H cell for evaluating LiPS shuttling. (h) Galvanostatic discharge profiles at 0.18 mA cm<sup>-2</sup> for CNT/S/APAF cathodes (S: 3.00 mg cm<sup>-2</sup>) and digital photos of H cells. (i) Galvanostatic discharge profiles at 0.18 mA cm<sup>-2</sup> for conventional cathodes (S: 3.00 mg cm<sup>-2</sup>) and digital photos of H cells.

Figure 2g, the CNT/S/APAF cathodes remain intact after being bent, demonstrating excellent mechanical properties. The crosssectional SEM image of the CNT/S/APAF cathode reveals the densely packed and layered structure of the self-supporting cathode obtained through vacuum filtration (Figure 2h). The magnified area highlights the interconnected framework with hierarchical pores (Figure 2i), which effectively facilitates electrolyte infiltration and ion transport while accommodating volume expansion during battery cycling. The sulfur content in the CNT/S/APAF cathode is 60.6% (Figure S8), and the uniform distribution of sulfur throughout the cathode is clearly shown in Figure S9. In contrast, the conventional S cathode contains an effective sulfur content of 60.0%, which decreases to 36.2% when the weight of the carbon-coated aluminum current collector is included. The bottom of the CNT/S/APAF cathode is a CNT film, which is composed of a continuous CNT network (Figure S10). Moreover, this free-standing and flexible composite sulfur cathode can be used directly without the need for an additional current collector and any conductive additives or binders. The as-prepared cathodes exhibited excellent electrolyte wettability and electrical conductivity. As shown in Figure 2j and Video S1, the electrolyte displays a 0° contact angle on the CNT/S/APAF cathodes and is quickly absorbed upon contact, indicating excellent electrolyte wettability. In contrast, the conventional cathodes show a much larger contact angle of 44.5°. The electrolyte uptake of APAF

(363.7%) is higher than that of AP (312.4%), further demonstrating its superior wettability with the electrolyte (Figure 2k). The electrical conductivities of CNT, impregnated once and twice, are 818.7 and  $1612~S~m^{-1}$ , respectively, enabling efficient charge transport (Figure 2l).

The improved electrolyte wettability and electrical conductivity in the cathodes are crucial for efficient ion-to-electron conduction and high sulfur utilization under low E/S ratio conditions. At high sulfur loadings, the Li-S reaction kinetics become extremely slow, as the ion and electron transport distances increase proportionally with sulfur loading. Moreover, under lean electrolyte conditions, concentrated LiPSs can significantly reduce the ionic conductivity, further hindering the reaction kinetics. These factors significantly affect the overall cell energy density and sulfur utilization.

**Evaluation of Sulfur Conversion Kinetics and LiPS Behavior in the Cathodes.** We evaluated the electrochemical kinetics in the high-loading cathodes using cyclic voltammetry (CV), galvanostatic intermittent titration technique (GITT), and electrochemical impedance spectroscopy (EIS) measurements. Figure 3a shows the CV test results of the Li–S cells at a scan rate of 0.05 mV s<sup>-1</sup>. Two reduction peaks at 2.29 and 1.96 V are attributed to the two-step reduction from sulfur to long-chain LiPSs and then to the final product, lithium sulfide (Li<sub>2</sub>S). The smaller polarization and larger peak current of the CNT/S/APAF cathodes compared to conventional cathodes indicate

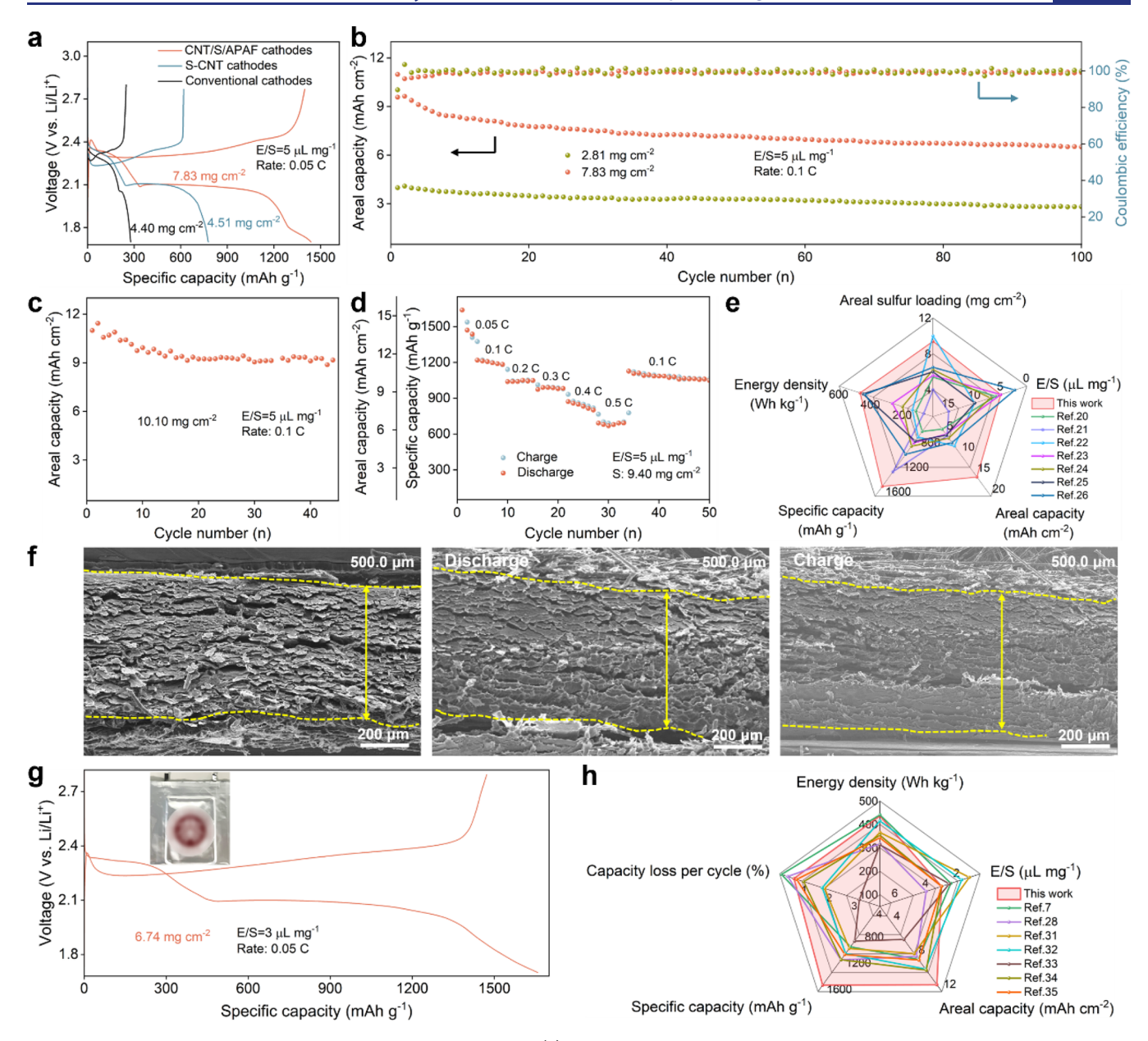


Figure 4. Electrochemical performance of CNT/S/APAF cathodes. (a) Galvanostatic discharge/charge profiles of the CNT/S/APAF, S-CNT, and conventional cathodes at 0.05 C. (b) Long-cycling performance of CNT/S/APAF cathodes under different sulfur loadings at 0.1 C. (c) Cycling performance of CNT/S/APAF cathodes with a high sulfur loading of 10.10 mg cm<sup>-2</sup> at 0.1 C. (d) Rate performance of CNT/S/APAF cathodes. (e) Comparison of the recently reported electrochemical performances of a Li–S coin cell. (f) Cross-sectional SEM image of CNT/S/APAF cathodes after 10 cycles at 0.1 C. (g) Galvanostatic discharge/charge profiles at 0.05 C of CNT/S/APAF cathodes (inset: a photograph of the as-fabricated CNT/S/APAF cathode-based Li–S pouch cell). (h) Comparison of the recently reported electrochemical performances of Li–S pouch cells.

accelerated redox kinetics. The absence of the reduction peak in conventional cathodes is associated with  $\text{Li}_2\text{S}$  formation, which further shows their sluggish redox kinetics. The corresponding Tafel plots of the reduction (peak A) and oxidation (peak B) peaks were calculated (Figure 3b and Figure S11). The low Tafel slopes of CNT/S/APAF cathodes verify their bidirectional catalytic activity, enabling rapid Li–S conversion. The lithiumion ( $\text{Li}^+$ ) diffusion coefficient ( $D_{\text{Li}}$ ) was evaluated by CV curves at different scan rates based on the Randles–Ševčík equation. The  $D_{\text{Li}}$  is related to the slope between the peak current and the square root of the sweeping rate ( $v^{0.5}$ ). It can be observed that the slope for CNT/S/APAF cathodes is higher, which benefits the sulfur reaction kinetics (Figure 3c and Figure S12).

Improved electrochemical kinetics were also determined by the galvanostatic intermittent titration technique (GITT) and electrochemical impedance spectroscopy measurements. As shown in Figure 3d,e, the CNT/S/APAF cathodes show lower polarization compared to conventional cathodes. The internal resistance, used to quantify the polarization, <sup>24</sup> reveals that CNT/S/APAF cathodes exhibit significantly lower internal resistance during the entire discharge process (Figure 3f). The lower charge transfer resistance ( $R_{\rm ct}$ ) of the CNT/S/APAF cathodes indicates superior charge transfer kinetics (Figure S13). These results demonstrate that CNT/S/APAF cathodes significantly enhance the electrochemical conversion of sulfur.

The Li-S H cell setup<sup>25</sup> was further employed to study LiPS shuttling in the Li-S cells using designed cathodes and the

conventional cathodes (Figure 3g). After discharge, the CNT/ S/APAF cathodes exhibited minimal LiPS shuttling, as evidenced by the negligible color change in the electrolyte (Figure 3h). In contrast, conventional cathodes induced significant LiPS shuttling, resulting in a visible color change (Figure 3i). While a slight color change was observed for the CNT/S/APAF cathodes, this likely originates from surfacelocalized solvation of polysulfides, which is known to facilitate sulfur redox kinetics and improve reaction reversibility rather than bulk dissolution. Such surface-confined solvation phenomena have been previously reported to benefit electrochemical performance.<sup>26</sup> To further quantify the extent of polysulfide diffusion, ultraviolet-visible (UV-vis) absorption spectroscopy was employed to determine the concentrations of LiPSs in the electrolyte from different cathodes after discharge. A standard calibration curve for Li<sub>2</sub>S<sub>6</sub> at 290 nm was established (Figure S14a,b). Based on this calibration, the electrolyte from the CNT/S/APAF cathodes showed a Li<sub>2</sub>S<sub>6</sub> concentration approximately 12.6 times lower than that of the conventional cathode (Figure S14c,d), confirming the strong polysulfide confinement capability of the CNT/S/APAF framework. This suppression is further supported by the lower polarization observed on the second discharge plateau compared with conventional cathodes. In addition, direct adsorption experiments using Li<sub>2</sub>S<sub>6</sub> solution demonstrated that APAF exhibits a significantly enhanced polysulfide adsorption capacity<sup>27</sup> (3.8 times higher than that of untreated aramid fibers) due to the introduction of functional groups via plasma treatment (Figure S15a,b). These results collectively demonstrate the strong polysulfide anchoring ability of the CNT/S/APAF structure. To further verify the chemical interactions between LiPSs and APAF, XPS analysis was performed on APAF after Li<sub>2</sub>S<sub>6</sub> adsorption. As shown in Figure S16, the S 2p spectrum was deconvoluted into peaks corresponding to sulfide (162.2 eV), S-S/S-C (163.7 and 164.9 eV), S-O (164.7 and 165.9 eV), and sulfate species, indicating the formation of chemical bonds between LiPSs and the APAF surface. Furthermore, density functional theory (DFT) calculations were carried out to compare the interaction strength of Li<sub>2</sub>S<sub>6</sub> with those of AF and APAF. As shown in Figure S17, the calculated binding energy of Li<sub>2</sub>S<sub>6</sub> on APAF is significantly higher than that on AF, confirming the enhanced chemical affinity of the functionalized surface. Collectively, these results demonstrate that the plasma-induced surface functionalization of aramid fibers significantly improves their ability to chemically anchor LiPSs, thereby effectively mitigating the shuttle effect.

**Li–S Cell Performance.** We paired the designed cathodes with ether-based electrolytes (DOL/DME with LiTFSI and LiNO<sub>3</sub>) and lithium metal anodes to formulate high-performance Li-S cells. A low E/S ratio of 5  $\mu$ L mg<sup>-1</sup> was utilized to enhance energy density while minimizing electrolyte consumption. The galvanostatic charge-discharge process was employed to evaluate the cell performance. As shown in Figure 4a, the CNT/S/APAF cathodes show two well-defined discharge plateaus at approximately 2.4 and 2.1 V, corresponding to the reduction of S to high-order LiPSs and further conversion to the final product  $\text{Li}_2\text{S}$ , respectively.<sup>28</sup> The higher initial discharge specific capacity of 1437.6 mAh g<sup>-1</sup> and areal capacity of 11.3 mAh cm<sup>-2</sup> with an S loading of 7.83 mg cm<sup>-2</sup> indicate enhanced S utilization and efficient reaction kinetics facilitated by the CNT/S/APAF cathodes. In contrast, cathodes fabricated using the conventional blade-coating method with a slurry (denoted as conventional cathodes) exhibit a significantly

lower discharge specific capacity of 277.4 mAh g<sup>-1</sup>, accompanied by pronounced polarization on the second discharge plateau. To provide a more appropriate baseline for comparison, a sulfur-carbon nanotube (S-CNT) cathode was prepared (see preparation details in the Supporting Information), and its electrochemical performance was evaluated under comparable conditions. The S-CNT cathodes delivered a significantly lower specific discharge capacity of 776.6 mAh  $g^{-1}$  at a sulfur loading of 4.51 mg cm<sup>-2</sup> (Figure 4a), highlighting the enhanced sulfur utilization and polysulfide confinement capability of the designed CNT/S/APAF architecture. Additionally, the longcycle performance of CNT/S/APAF cathodes was evaluated. The discharge capacities of 6.51, 6.38, and 2.82 mAh cm<sup>-2</sup> are maintained after 100 cycles with average CEs of 98.99, 99.24, and 99.72% at S loadings of 7.83, 6.56, and 2.81 mg cm<sup>-2</sup>, respectively, whereas the S-CNT cathodes exhibited a significantly lower areal capacity of only 1.93 mAh cm<sup>-2</sup> after 100 cycles (Figure S18). A discharge areal capacity of 9.17 mAh cm<sup>-2</sup> was retained after 44 cycles at a high sulfur loading of 10.10 mg cm<sup>-2</sup> (Figure 4c). The excellent cycling stability is attributed to the well-designed encapsulation structure and the flexibility of CNT and AF. The rate performance of CNT/S/APAF cathodes was evaluated from 0.1 to 0.5 C at a sulfur loading of 9.40 mg cm<sup>-2</sup>. The discharge capacities are 1219.4, 1039.2, 973.8, 871.2, and 691.2 mAh g<sup>-1</sup>, and areal capacities are 11.46, 9.77, 9.15, 8.19, and 6.50 mAh cm<sup>-2</sup> at current densities of 0.1, 0.2, 0.3, 0.4, and 0.5 C, respectively, and recovers to 1126.5 mAh  $g^{-1}$  (10.60 mAh cm<sup>-2</sup>) when returning to 0.1 C (Figure 4d), indicating excellent rate reversibility. To further evaluate the rate capability under a broader range of operating conditions, the CNT/S/ APAF cathodes were tested at current densities ranging from 0.1 to 2.5 C with a sulfur loading of 5.50 mg cm<sup>-2</sup>. As shown in Figure S19, the cathodes deliver discharge capacities of 1625.7, 1280.1, 1027.8, 608.9, 524.5, and 465.8 mAh g<sup>-1</sup> at 0.1, 0.5, 1.0, 1.5, 2, and 2.5 C, respectively. When the current density was returned to 0.5 C, the discharge capacity recovered to 1126.5 mAh g<sup>-1</sup>, further confirming the good rate performance and structural integrity of the CNT/S/APAF cathodes. Moreover, a high energy density of 468.6 Wh kg<sup>-1</sup> (based on the weight of the cathode including the current collector, electrolyte, separator, and Li; Table S2) was achieved at a sulfur loading of 9.40 mg cm<sup>-2</sup>, surpassing most reported works (Figure 4e and Table S3). 16,29-35 Cross-sectional SEM images (Figure 4f) reveal that CNT/S/APAF cathodes effectively accommodate large volume changes while maintaining a consistent electrode thickness. In contrast, conventional cathodes experience substantial volume changes during cycling (Figure S20).

We fabricated a pouch cell using a single-piece CNT/S/APAF cathode (3.5  $\times$  3.5 cm) with a sulfur loading of 6.74 mg cm<sup>-2</sup>. The as-prepared pouch cell was activated at a current density of 0.05 C and cycled at a current density of 0.1 C with an E/S ratio of 3  $\mu$ L mg<sup>-1</sup>. It delivers an initial discharge specific capacity of 1658.7 mAh g<sup>-1</sup> with a capacity loss per cycle of 0.57% and high CE of 99.03% for 19 cycles (Figure 4g and Figure S21). The Li-S pouch cell delivers 436.9 Wh kg<sup>-1</sup> cell-level energy density (based on the weight of the cathode including the current collector, electrolyte, separator, and Li), demonstrating the practical value of the CNT/S/APAF cathode (Table S4). Compared with previously reported results from other Li-S pouch cells based on cell configuration optimization, our designed CNT/S/APAF cathodes demonstrate a remarkable enhancement in energy density and cycle life (Figure 4h and Table S5). 7,33,36-40 We also evaluated the volumetric performance of the CNT/S/APAF cathode by investigating its compressibility. Owing to the mechanical resilience of the APAF scaffold and the conformal CNT/S coating, the cathode thickness can be reduced from  $\sim$ 500 to  $\sim$ 53  $\mu$ m under moderate mechanical pressure, corresponding to a compression ratio of 89.4% (Figure S22). Importantly, this compression does not compromise the structural integrity or electrochemical performance. Upon release of the applied pressure, the thickness recovers to  $\sim$ 438  $\mu$ m, confirming its reversible compressibility. This compressible feature allows electrode densification without performance degradation, offering a promising strategy to enhance the volumetric energy density of practical Li-S batteries. Furthermore, extended cycling tests were conducted at an elevated current density of 0.6 C. At a sulfur loading of 5.10 mg cm<sup>-2</sup>, the CNT/S/APAF cathodes maintained a discharge capacity of 591.8 mAh g<sup>-1</sup> after 130 cycles (Figure S23), demonstrating good electrochemical cycling stability.

These findings demonstrate that the synergistic effect of the CNT network, the active functional groups in APAF, and the unique encapsulation structure effectively promote efficient electron transport, improve electrolyte wettability, inhibit LiPS shuttling, and mitigate volume expansion, thereby enhancing energy density and cycling stability.

## CONCLUSIONS

In summary, we successfully fabricated a free-standing, flexible sulfur cathode by integrating a regulated electronic and ionic conductive framework into a CNT network, where the framework was constructed by CNT and sulfur onto air plasma-treated aramid fibers in a layer-by-layer fashion. This innovative structure effectively enhances electron transport, improves electrolyte wettability, suppresses polysulfide diffusion, and mitigates volume expansion, addressing key challenges in high energy density Li-S batteries. As a result, these cathodes demonstrate exceptional electrochemical performance and remarkable cycling stability even under lean electrolyte conditions. Furthermore, their compatibility with scalable, continuous production offers a practical pathway for advancing Li-S battery technology, enabling next-generation energy storage systems with high energy density and long-term reliability.

### ASSOCIATED CONTENT

# **Supporting Information**

The Supporting Information is available free of charge at https://pubs.acs.org/doi/10.1021/jacs.5c07454.

Experimental procedures, materials, methods, characterization data, additional electrochemical measurements, and computational details; schematic illustration of the experimental setup (PDF)

Contact angle measurement video of the CNT/S/APAF cathodes (MP4)

# AUTHOR INFORMATION

## **Corresponding Author**

Xin Gao — School of Materials Science and Engineering, Peking University, Beijing 100871, P. R. China; Beijing Graphene Institute (BGI), Beijing 100095, P.R. China; orcid.org/0000-0001-5360-0796; Email: gaoxin-cnc@pku.edu.cn

#### **Authors**

Xueting Feng — School of Materials Science and Engineering and Beijing Science and Engineering Center for Nanocarbons, Beijing National Laboratory for Molecular Sciences, College of Chemistry and Molecular Engineering, Peking University, Beijing 100871, P. R. China

Xuanguang Ren — School of Materials Science and Engineering and Beijing Science and Engineering Center for Nanocarbons, Beijing National Laboratory for Molecular Sciences, College of Chemistry and Molecular Engineering, Peking University, Beijing 100871, P. R. China; Beijing Graphene Institute (BGI), Beijing 100095, P.R. China

Huahui Tian — Beijing Graphene Institute (BGI), Beijing 100095, P.R. China; State Key Laboratory of High-Efficiency Coal Utilization and Green Chemical Engineering, College of Chemistry and Chemical Engineering, Ningxia University, Yinchuan 750021, P. R. China

Mingwei Cui — Beijing Science and Engineering Center for Nanocarbons, Beijing National Laboratory for Molecular Sciences, College of Chemistry and Molecular Engineering, Peking University, Beijing 100871, P. R. China

**Guoxin Lu** – School of Materials Science and Engineering, Peking University, Beijing 100871, P. R. China

Jin Zhang — School of Materials Science and Engineering and Beijing Science and Engineering Center for Nanocarbons, Beijing National Laboratory for Molecular Sciences, College of Chemistry and Molecular Engineering, Peking University, Beijing 100871, P. R. China; Beijing Graphene Institute (BGI), Beijing 100095, P.R. China; orcid.org/0000-0003-3731-8859

Complete contact information is available at: https://pubs.acs.org/10.1021/jacs.5c07454

### **Author Contributions**

"X.F., X.R., and H.T. contributed equally.

#### Notes

The authors declare no competing financial interest.

# ACKNOWLEDGMENTS

This work was financially supported by the National Natural Science Foundation of China (grant nos. 52302034, 52021006, and 52402041), the National Key R&D Program of China (2022YFA1203302 and 2022YFA1203304), the Strategic Priority Research Program of CAS (XDB36030100), the Beijing National Laboratory for Molecular Sciences (BNLMS-CXTD-202001), and the China Postdoctoral Science Foundation (grant nos. 8206300625 and 8206400103).

#### REFERENCES

- (1) Pang, Q.; Liang, X.; Kwok, C. Y.; Nazar, L. F. Advances in lithium—sulfur batteries based on multifunctional cathodes and electrolytes. *Nature Energy* **2016**, *1*, 16132.
- (2) Zhou, S.; et al. Visualizing interfacial collective reaction behaviour of Li-S batteries. *Nature* **2023**, *621*, 75–81.
- (3) Liu, R.; et al. Establishing reaction networks in the 16-electron sulfur reduction reaction. *Nature* **2024**, *626*, 98–104.
- (4) Peng, L.; et al. A fundamental look at electrocatalytic sulfur reduction reaction. *Nature Catalysis* **2020**, *3*, 762–770.
- (5) Wu, J.; et al. From Fundamental Understanding to Engineering Design of High-Performance Thick Electrodes for Scalable Energy-Storage Systems. *Adv. Mater.* **2021**, *33*, No. e2101275.

- (6) Liu, X.; Huang, J. Q.; Zhang, Q.; Mai, L. Nanostructured Metal Oxides and Sulfides for Lithium-Sulfur Batteries. *Adv. Mater.* **2017**, 29, 1601759.
- (7) Zhao, C.; et al. A high-energy and long-cycling lithium-sulfur pouch cell via a macroporous catalytic cathode with double-end binding sites. *Nat. Nanotechnol.* **2021**, *16*, 166–173.
- (8) Xu, J.; et al. Sandwiched cathodes kinetically boosted by few-layered catalytic 1T-MoSe<sub>2</sub> nanosheets for high-rate and long-cycling lithium-sulfur batteries. *EcoMat* **2023**, *S*, No. e12329.
- (9) Lee, H.; Nam, H.; Moon, J. H. Seamless integration of nanoscale crystalline-amorphous MoO3 domains for high-performance lithium-sulfur batteries. *Energy Storage Materials* **2024**, *70*, No. 103551.
- (10) Peng, H. J.; Huang, J. Q.; Cheng, X. B.; Zhang, Q. Review on High-Loading and High-Energy Lithium—Sulfur Batteries. *Adv. Energy Mater.* **2017**, *7*, 1700260.
- (11) Zhou, G.; Chen, H.; Cui, Y. Formulating energy density for designing practical lithium—sulfur batteries. *Nature Energy* **2022**, *7*, 312–319.
- (12) Wang, M.; et al. Advances in High Sulfur Loading Cathodes for Practical Lithium-Sulfur Batteries. *Adv. Energy Mater.* **2022**, *12*, 2201585.
- (13) Zhao, M.; et al. Lithium-Sulfur Batteries under Lean Electrolyte Conditions: Challenges and Opportunities. *Angew. Chem., Int. Ed. Engl.* **2020**, *59*, 12636–12652.
- (14) Yeom, S.; Jo, H.; Lee, H.; Moon, J. H. Lithiating cathodes for Li-S batteries: Regulating Li2S electrodeposition to enhance sulfur utilization. *Energy Storage Materials* **2024**, *71*, No. 103644.
- (15) Zhao, M.; Li, B. Q.; Zhang, X. Q.; Huang, J. Q.; Zhang, Q. A Perspective toward Practical Lithium-Sulfur Batteries. ACS Central Science 2020, 6, 1095–1104.
- (16) Guo, Q.; et al. A Freestanding, Dissolution- and Diffusion-Limiting, Flexible Sulfur Electrode Enables High Specific Capacity at High Mass Loading. *Adv. Mater.* **2024**, *36*, No. e2400041.
- (17) Zhang, H.; Ono, L. K.; Tong, G.; Liu, Y.; Qi, Y. Long-life lithium-sulfur batteries with high areal capacity based on coaxial CNTs@TiN-TiO2 sponge. *Nature Communication* **2021**, *12*, 4738.
- (18) Um, K.; et al. Janus architecture host electrode for mitigating lithium-ion polarization in high-energy-density Li–S full cells. *Energy Environ. Sci.* **2024**, *17*, 9112–9121.
- (19) Jeon, D.; et al. Electrospun Carbon Nanofibers for Clean Energy Applications: A Comprehensive Review. *EcoMat* **2025**, *7*, No. e12517.
- (20) Han, P.; Chung, S.-H.; Manthiram, A. Designing a high-loading sulfur cathode with a mixed ionic-electronic conducting polymer for electrochemically stable lithium-sulfur batteries. *Energy Storage Materials* **2019**, *17*, 317–324.
- (21) Zhang, H.; et al. Aramid nanofiber-based functional composite materials: Preparations, applications and perspectives. *Composites Part B: Engineering* **2024**, 271, No. 111151.
- (22) Jia, C.; et al. Effects of Twaron fiber surface treatment by air dielectric barrier discharge plasma on the interfacial adhesion in fiber reinforced composites. *Surf. Coat. Technol.* **2010**, 204, 3668–3675.
- (23) Wu, K.; et al. Highly efficient and green fabrication of a modified C nanofiber interlayer for high-performance Li—S batteries. *Journal of Materials Chemistry A* **2018**, *6*, 2693—2699.
- (24) Park, J.; et al. The Importance of Confined Sulfur Nanodomains and Adjoining Electron Conductive Pathways in Subreaction Regimes of Li-S Batteries. *Adv. Energy Mater.* **2017**, *7*, 1700074.
- (25) Chen, H.; et al. Electrode Design with Integration of High Tortuosity and Sulfur-Philicity for High-Performance Lithium-Sulfur Battery. *Matter* **2020**, *2*, 1605–1620.
- (26) Liu, Y.; et al. Surface-localized phase mediation accelerates quasi-solid-state reaction kinetics in sulfur batteries. *Nat. Chem.* **2025**, *17*, 614–623.
- (27) Oh, K.; Nam, H.; Jang Chung, Y.; Hyuk Moon, J. Dry carbothermal reaction-enabled ultra-dense nanoparticle coatings for high-performance Li-S batteries. *Chemical Engineering Journal* **2024**, 499, No. 156229.

- (28) Chung, S. H.; Manthiram, A. Current Status and Future Prospects of Metal-Sulfur Batteries. *Adv. Mater.* **2019**, *31*, No. e1901125.
- (29) Yuan, Y.; et al. Encapsulating Various Sulfur Allotropes within Graphene Nanocages for Long-Lasting Lithium Storage. *Adv. Funct. Mater.* **2018**, 28, 1706443.
- (30) Luo, L.; Li, J.; Yaghoobnejad Asl, H.; Manthiram, A. In-Situ Assembled VS4 as a Polysulfide Mediator for High-Loading Lithium—Sulfur Batteries. *ACS Energy Letters* **2020**, *5*, 1177—1185.
- (31) Cheng, X.-B.; et al. Aligned carbon nanotube/sulfur composite cathodes with high sulfur content for lithium—sulfur batteries. *Nano Energy* **2014**, *4*, 65–72.
- (32) Liu, J.; et al. Hollow urchin-like Mn<sub>3</sub>O<sub>4</sub> microspheres as an advanced sulfur host for enabling Li-S batteries with high gravimetric energy density. *J. Journal of Colloid and Interface Science* **2022**, 606, 1111–1119.
- (33) Xue, W.; et al. Intercalation-conversion hybrid cathodes enabling Li–S full-cell architectures with jointly superior gravimetric and volumetric energy densities. *Nature Energy* **2019**, *4*, 374–382.
- (34) Agostini, M.; et al. Minimizing the Electrolyte Volume in Li–S Batteries: A Step Forward to High Gravimetric Energy Density. *Adv. Energy Mater.* **2018**, *8*, 1801560.
- (35) Zhong, M. e.; et al. A Cost- and Energy Density-Competitive Lithium-Sulfur Battery. *Energy Storage Materials* **2021**, *41*, 588–598.
- (36) Li, Z.; et al. Lithiated metallic molybdenum disulfide nanosheets for high-performance lithium—sulfur batteries. *Nature Energy* **2023**, 8, 84—93
- (37) Xie, Y.; et al. Semi-Flooded Sulfur Cathode with Ultralean Absorbed Electrolyte in Li-S Battery. *Advanced Science* **2020**, *7*, 1903168.
- (38) Shi, L.; et al. Reaction heterogeneity in practical high-energy lithium—sulfur pouch cells. *Energy Environ. Sci.* **2020**, *13*, 3620–3632.
- (39) Peng, Y. Q.; et al. Full-Range Redox Mediation on Sulfur Redox Kinetics for High-Performance Lithium-Sulfur Batteries. *Batteries & Supercaps* **2022**, *5*, No. e202100359.
- (40) Zhao, C. X.; et al. Semi-Immobilized Molecular Electrocatalysts for High-Performance Lithium-Sulfur Batteries. *J. Am. Chem. Soc.* **2021**, 143, 19865—19872.